Forward and inverse kinetic energy cascades in Jupiter's turbulent weather layer

Roland M. B. Young[1*] & Peter L. Read[1]

[1]*Atmospheric, Oceanic and Planetary Physics, Department of Physics, University of Oxford, UK*
[*]Corresponding author.

Jupiter's turbulent weather layer contains phenomena of many different sizes, from local storms up to the Great Red Spot and banded jets. The global circulation is driven by complex interactions with (as yet uncertain) small scale processes. We have calculated structure functions and kinetic energy spectral fluxes from Cassini observations over a wide range of length scales in Jupiter's atmosphere. We found evidence for an inverse cascade of kinetic energy from length scales comparable with the first baroclinic Rossby deformation radius to the global jet scale, but also a forward cascade of kinetic energy from the deformation radius to smaller scales. The latter disagrees with the traditional picture of Jupiter's atmospheric dynamics, but has some similarities with mesoscale phenomena in the Earth's atmosphere and oceans. We conclude that the inverse cascade driving Jupiter's jets may have a dominant energy source at scales close to the deformation radius, such as baroclinic instability.

With a typical Reynolds number of $\sim 10^{13}$ and Rossby number of ~ 0.01, Jupiter's atmosphere is one of the most turbulent places in the Solar System [1–3], and is an excellent natural example of quasi-2D, rotating, stratified turbulence. Its turbulent weather layer is obvious from even the most cursory examination, with eddies over a wide range of length scales from the $40\,000\,\mathrm{km}$ diameter Great Red Spot down to the pixel scale in high resolution images (Fig. 1).

[Figure 1 about here]

A distinctive characteristic of a turbulent flow is the nonlinear transfer of energy, vorticity and other flow properties between different scales of motion in processes known as *cascades*. In homogeneous, isotropic 3D turbulence, for example, nonlinear exchanges tend to cascade kinetic energy from large to small scales, where it may be removed by viscous dissipation, leading to the well known Kolmogorov $-\frac{5}{3}$ law for the kinetic energy spectrum in the inertial range at intermediate scales [4]. In contrast, in a two-dimensional or quasi-geostrophic system forced at a given scale L_f, the "classical" picture [5–8] suggests that energy will generally cascade towards scales $\geq L_f$ while enstrophy (squared relative vorticity) cascades to scales $\leq L_f$, exhibiting self-similar energy spectra with slopes of $-\frac{5}{3}$ and -3 respectively.

In a rapidly rotating, stably stratified planetary atmosphere, such as on Earth or Jupiter, the situation is likely to be more complicated, but it is now well established [9] that the Earth's upper troposphere exhibits a steep spectrum at synoptic scales ($\sim$1000–5000 km) with a slope close to -3. This may suggest a classical downscale enstrophy-dominated cascade, although spectral flux determinations [10–12] indicate that energy is mostly transferred upscale. At smaller scales, however, the energy spectrum becomes significantly shallower, with a slope approaching the Kolmogorov-like value of $-\frac{5}{3}$, the interpretation of which remains controversial [13–18]. The $-\frac{5}{3}$ slope is consistent with both the inverse energy cascade of classical 2D turbulence [14] and a spectrum of internal gravity waves with a forward energy cascade to small scales [13], and so its interpretation depends crucially on measuring the direction and magnitude of the cascades of energy and enstrophy over this range of scales.

In determining this, several authors [19–22] have used methods based on the structure function which entails computing various two-point covariances of velocity as a function of separation. These appear to show a downscale energy transfer over the range of scales where the $-\frac{5}{3}$ spectrum is found, although the debate continues as to which mechanism may be responsible. A similar reversal in the direction of the kinetic energy cascade is also evident in the oceans [23,24] around the scale of the first baroclinic deformation radius, likely consistent with an injection of kinetic energy associated with baroclinic instability.

On Jupiter, although several authors [25–28] have made determinations of the sense and magnitude of the conversion rate of kinetic energy from eddies into zonal jets from cloud wind measurements, the cascade of kinetic energy associated with eddy-eddy interactions has remained largely unexplored in observations until the present work. Here we measure the direction of Jupiter's kinetic energy cascade throughout the range of observed length scales using

Author post-print. Manuscript accepted for publication in *Nature Physics*.

both structure functions[19,20] and spectral fluxes[10,11,29] as complementary approaches. The prevailing view[3] would anticipate that, given the strong dominance of planetary rotation on large-scale motions on Jupiter, energy is likely to be mostly transferred upscale from the relatively small scales (dominated by convection or baroclinic instabilities) towards the scales of the zonal bands[30,31]. Of particular interest in this context is the trend towards a $-\frac{5}{3}$ spectrum at the smallest resolvable scales in kinetic energy derived from cloud motions[27], which suggests an energy-dominated inertial range but with an uncertain direction of the associated energy cascade.

Jupiter wind maps derived from Cassini flyby observations

NASA's Cassini spacecraft flew by Jupiter in December 2000, and took a large number of images in the visible and near-infrared (IR) bands using the Imaging Science Subsystem (ISS) instrument[32] (Fig. 1). A short subset of the images before closest approach have been pre-processed, projected onto a longitude-latitude grid, and made available for public use[33]. We use horizontal winds calculated by two independent cloud tracking analyses of the CB2 near-IR continuum band images[27,28]. Datasets G14g[27] and C11[28] contain global zonal (u) and meridional (v) wind velocity fields on latitude-longitude grids, covering three rotation periods of the planet over 360° longitude and $\pm 50^\circ$ latitude. We also use a third dataset, G14s, which contains local wind vector fields covering almost four rotation periods, each one including the raw velocity vectors from one of the 70 image pairs (approximately a square of side 60–70°) that were subsequently stitched together to construct the G14g dataset.

2nd and 3rd order turbulent structure functions

Using dataset G14s we calculated the 2nd and 3rd order structure functions for flow in Jupiter's weather layer. The 3rd order structure function identifies the direction of kinetic energy propagation between different length scales, and quantifies the rate at which energy moves through a turbulent cascade. It is calculated from the cube of the velocity difference projected along a line separating two points, δu_L, as a function of the separation distance r between those two points, averaged over all possible pairs of points. For 3D homogeneous isotropic turbulence the 3rd order longitudinal structure function, suitably averaged over time and space, is negative and in the Kolmogorov inertial range varies linearly as $\langle \delta u_L^3 \rangle = -\frac{4}{5}\epsilon r$, where ϵ is the energy injection rate at large scales[34]. In the energy inertial range of a 2D turbulent flow, however, a homogeneous isotropic flow is expected to exhibit positive 3rd order longitudinal and transverse structure functions $\langle \delta u_L^3 \rangle = +\frac{3}{2}Pr$ and $\langle \delta u_L \delta u_T^2 \rangle = +\frac{1}{2}Pr$, where P is the energy input power due to a small-scale driving force[19], and δu_T is the velocity difference projected perpendicular to the separation vector. Hence the 3rd order structure function can reveal both the direction and, to some extent, the magnitude of the turbulent energy flux in Jupiter's weather layer.

[Figure 2 about here]

Figure 2a shows the 3rd order structure functions for flow in Jupiter's weather layer, as a function of separation distance, averaging over all separation directions. There is a well-defined linear and positive dependence of the structure functions on r between separations of 3500–40 000 km. The positive structure functions show there is an upscale energy flux over these scales, from small to large scales, and the linear trend in r indicates there may be a self-similar inverse energy cascade akin to the $-\frac{5}{3}$ cascade of classical 2D turbulence in its inertial range. We fitted $\langle \delta u_L^3 \rangle = +\frac{3}{2}Pr$ and $\langle \delta u_L \delta u_T^2 \rangle = +\frac{1}{2}Pr$ to the data between $0 \le r \le 50\,000\,\mathrm{km}$ and found the energy input power to be $P \approx 1 \times 10^{-4}\,\mathrm{W\,kg^{-1}}$. Only a rough estimate of the magnitude of the input power is justified using this method, however. The fits assume homogeneous isotropic turbulence, and at large scales at least Jupiter's atmosphere is anisotropic. While the structure functions are qualitatively the same independent of direction, we find P varies by up to a factor of five when comparing separations in the East-West and North-South directions, which points to flow anisotropy in physical space (Supplementary Fig. 7). Therefore we quote P to its leading digit only. This estimate is somewhat larger than our earlier estimate of $\epsilon = (0.5 - 1.0) \times 10^{-5}\,\mathrm{W\,kg^{-1}}$, measured directly from the kinetic energy spectrum[27], but this is possibly because that work used a mosaicing procedure that damps the eddy velocities (Supplementary Fig. 5), and also the Kolmogorov constant used in the fit to find ϵ in that work is not well known on the sphere. Our figure does agree well with eddy-zonal kinetic energy conversion rates of $(0.7 - 3.0) \times 10^{-4}\,\mathrm{W\,kg^{-1}}$ calculated from eddy momentum flux analyses[25,26].

Author post-print. Manuscript accepted for publication in *Nature Physics*.

It is the behaviour at small scales $r < 3500\,\mathrm{km}$ that is particularly intriguing, however. Here the 3rd order longitudinal structure function is negative, implying downscale energy transfer from large to small scales, in contrast to the traditional picture of Jupiter's atmospheric turbulence. It clearly does not vary as $-r$ as in standard 3D turbulence, but energy flux diverging both upscale and downscale from a small range of length scales implies these length scales contain a significant kinetic energy source for the flow. The only relevant length scale close to this scale is the first baroclinic Rossby deformation radius, L_D, which is the horizontal scale where the effects of rotation and stratification are comparable, and is also the size of typical baroclinic eddies. For typical midlatitudes $\phi = 20-40^\circ$ the deformation radius likely ranges from 1500–$3500\,\mathrm{km}$ (See Supplementary Information, and Fig. 1).

Figure 2b shows the 2nd order structure functions. At small scales $< L_D$ these approach the classical $r^{2/3}$ form for a 2D turbulent flow with $-\frac{5}{3}$ energy spectrum. However, between L_D and L_{jet} the structure function is close to flat, not $r^{2/3}$ as expected in the energy-dominated inertial range of 2D turbulence[19]. The eddy kinetic energy spectrum, which is shown in Fig. 3a, is reasonably well approximated by a flat spectrum at low wavenumbers and a $n^{-5/3}$ spectrum at high wavenumbers, with a transition around $n \sim 80$. Such a spectrum results in a 2nd order structure function that is flat at large r, transitions around the break in the spectrum from flat towards $r^{2/3}$, and only approaches $r^{2/3}$ asymptotically at small r. In this case a good $r^{2/3}$ fit is only expected for $r \lesssim 1000\,\mathrm{km}$. This relationship is derived in the Supplementary Information (Supplementary Figs 1–4 and Supplementary Table 1). Our measured 2nd order structure functions are qualitatively consistent with this picture and hence, despite their deviation from the classical $r^{2/3}$, are consistent with our other results. The large-scale spectrum influences the small-scale structure function because it incorporates the energy contained in eddies of size r or less, plus r^2 times the enstrophy in eddies of size r or greater[35].

Spectral fluxes of kinetic energy and enstrophy

To corroborate our finding of downscale energy transfer at small scales in Jupiter's atmosphere, we computed the spectral fluxes of kinetic energy and enstrophy between different length scales directly. Using datasets G14g and C11 we calculated spectral fluxes on the sphere using a well-established method used for Earth[10,11]. Using dataset G14s we computed an independent estimate of the spectral fluxes by calculating nonlinear triad interactions[29], after projecting the velocity field for each image pair onto a plane. Because of the approximations required to project from the sphere to the plane, this third measurement should be considered a check on the first two measurements on the sphere (as it happens, the spectral fluxes agree well).

In all three cases we used the rotational (non-divergent) part of the horizontal velocity field only, when calculating the fluxes. Using a method that included the divergent terms[12], we found that the divergent parts of the G14g and C11 energy spectra differed significantly, while the rotational parts agreed well. We expect the error in the divergent part of the flow to be somewhat larger than the rotational part, therefore, and have omitted it in this analysis, but may examine it more closely in the future.

[Figure 3 about here]

Figure 3 shows the kinetic energy and enstrophy spectra and spectral fluxes. When the full velocity is considered, including the divergent component, the eddy kinetic energy spectrum (Fig. 3a) scales as the classical $n^{-5/3}$ for $n \gtrsim 80$ (note that the structure functions above used the full velocities). In the rotational component of the flow, the eddy part of the energy spectrum (Fig. 3b) appears to scale as n^{-2} for $n \gtrsim 80$. We note that a n^{-2} spectrum of rotational kinetic energy has also been reproduced in Earth atmosphere models in the upper troposphere[36]. The zonal part of the spectrum (Supplementary Fig. 10) gives us a heuristic estimate of the global jet scale, which is shown as a light grey band and corresponds to the peaks in the zonal energy spectrum of the three datasets near the jet scale: $n_{\mathrm{Jet}} = 23 - 28$. This corresponds to a typical latitudinal jet width of 8000–$9500\,\mathrm{km}$, as one wavelength is equivalent to two jets (Fig. 1).

Figure 3c shows the kinetic energy spectral flux calculated from the three datasets. There is good agreement between all three, particularly at small scales. Positive spectral flux corresponds to energy transfer from large to small scales, and the general trends are clear. First, the kinetic energy flux is negative and approximately flat (within a factor of two) between 4000–$15\,000\,\mathrm{km}$ length scales, suggesting there is an inverse cascade of kinetic energy with power $\Pi_{\mathrm{up}}^{\mathrm{E,tot}} \approx (-5\pm2)\times10^{-5}\,\mathrm{W\,kg^{-1}}$ from small scales up to the jet scale. The position and magnitude

Author post-print. Manuscript accepted for publication in *Nature Physics*.

of the inverse cascade agree broadly with the 3rd order structure function (Fig. 2a). Second, at small scales $\leq 2000\,\mathrm{km}$ the positive spectral flux corroborates our earlier finding of downscale energy transfer at small scales in the 3rd order structure function. There is a remarkable agreement between the three datasets on the length scale at which the switch from an upscale to a downscale flux occurs, and the agreement between this scale and a typical deformation radius in midlatitudes is striking. We cannot estimate the downscale flux reliably from our structure functions, but we can make a tentative estimate from the spectral fluxes. There is a small range of scales where the spectral flux is approximately flat, indicating an inertial range containing a forward energy cascade with power $\Pi^{\mathrm{E,tot}}_{\mathrm{down}} \approx (1.5 \pm 0.3) \times 10^{-5}\,\mathrm{W\,kg^{-1}}$. Third, Fig. 3d shows the kinetic energy spectral flux due to eddy-eddy interactions only. This has the same general form as the total energy flux, with inverse cascade power $\Pi^{\mathrm{E,ee}}_{\mathrm{up}} \approx (-0.8 \pm 0.6) \times 10^{-5}\,\mathrm{W\,kg^{-1}}$. So while most of the flux is due to zonal-eddy interactions, a not insubstantial part is due to eddy-eddy interactions. Finally, there is a convergence of kinetic energy at the jet scale. This comes both from larger scales (up to around $40\,000\,\mathrm{km}$) down to the jet scale and from smaller scales (down to around $2500\,\mathrm{km}$) up to the jet scale. We are not aware of any modelling work that reproduces such a downscale energy flux at large scales, although we do note there is also a weak convergence of kinetic energy at large scales in both the Earth's atmosphere[10] and oceans[23]. All three datasets show that the primary eddy to zonal flow energy conversion occurs at or near the jet scale (Fig. 3e).

The spectral enstrophy flux in Fig. 3f is overwhelmingly downscale, increasing strongly with wavenumber up to the resolution limit of the measurements. This is broadly consistent with expectations for quasi-geostrophic turbulence[7,8] and similar to what has been found for the Earth's atmosphere[10,11] but with no evidence for an enstrophy-cascading inertial range. Rather, there appears to be continuous generation of enstrophy at all scales smaller than the jet scale, suggestive of frontogenetic processes and filamentation of vorticity.

Implications for turbulence in Jupiter's atmosphere

The overall picture that emerges from our analysis is of a turbulent upper troposphere on Jupiter in which kinetic energy is generated on a scale comparable with the internal Rossby radius of deformation and cascades to both larger and smaller scales. At the same time, enstrophy is cascaded uniformly downscale but also generated over a wide range of scales down to the resolution limit of the observations.

Although the kinetic energy spectrum ends up looking superficially rather like what is seen in the Earth's upper troposphere, with a shallow $n^{-5/3}$ spectrum at small scales associated with a downscale energy cascade, the reversal of the energy cascade at a scale comparable with the Rossby radius is quite different and may suggest a rather different dynamical mechanism at work, perhaps more like the oceans[23,24]. In the Earth's atmosphere, mechanisms most frequently discussed for the reversal of the energy cascade are either forced gravity wave turbulence[13] or other forms of stably stratified vortical turbulence[17]. Aspects of the small scale behaviour resemble turbulence in Earth's atmosphere and oceans, but the flattening of the spectrum at large scales is distinctly non-terrestrial. Part of the upscale cascade covers this flatter region. We are not aware of any theory that explains such a cascade within a flat energy spectrum, and hence Jupiter's turbulence may not represent a "classical" inertial range. We hope this result will prompt others to think further about the underlying mechanisms.

On Jupiter, the Rossby deformation radius is rather too large to be consistent with an energy injection due to (dry or moist) convection, even though this may be energetically significant (at least locally) for the atmosphere as a whole[37,38], but more likely suggests a role for baroclinic instability. In the absence of a solid surface, however, such an instability will be somewhat different in character from its form in the Earth's atmosphere and may be more concentrated near the tropopause on Jupiter, where the static stability changes rapidly with height. This effectively forms a quasi-boundary where potential vorticity gradients may become large. Under these conditions, the flow near the tops of the clouds may be tracing something closer to a surface quasi-geostrophic (SQG) circulation[16,39–41], for which a reversal of the energy cascade is predicted to occur around the first baroclinic deformation radius, as found here for Jupiter.

This is not the only possibility, however, and a lot depends on what the energy cascade may be doing at deeper levels in Jupiter's troposphere. But if SQG dynamics underly the turbulence observed near Jupiter's cloud tops then there may be a strong signature in the temperature field near the tropopause[40], and perhaps a n^{-3} signal in the kinetic energy spectrum at deeper levels[41]. These may be observable in principle via remote sensing from orbit, but will require much higher spatial resolution thermal measurements of Jupiter's tropopause and lower stratosphere (better

Author post-print. Manuscript accepted for publication in *Nature Physics*.

than 1° in latitude and longitude) than have been available to date. Nevertheless, the existing measurements presented here provide important new constraints against which to compare dynamical models of Jupiter's troposphere.

Methods

Retrieval of wind velocities. Different cloud tracking algorithms based on Correlation Imaging Velocimetry (CIV) were used to retrieve wind vectors in each dataset. CIV compares patches of pixel brightnesses between images taken some time apart. The displacement and distortion of a pixel patch between the first and second images that maximises the 2D correlation coefficient gives an estimate of the fluid's displacement and hence its velocity[42,43]. The different datasets used different assumptions and additional steps, and the reader is referred to the relevant publications for details[27,28].

Dataset G14 is available in two forms. G14g contains four global (360° longitude, $\pm 50^\circ$ latitude) horizontal velocity mosaics on a 0.5° grid, one for each Jupiter rotation during the flyby, although we only use the first three for the spectral fluxes as there is a large longitudinal gap in the fourth mosaic. G14g is already publicly available[27]. G14s omits the final step of the cloud tracking procedure, which combined velocity vectors from individual image pairs onto a regular, global, grid. Instead, G14s retains the irregularly-spaced individual velocity vectors produced by the CIV procedure (1 123 505 in total), in 70 blocks corresponding to the images they were calculated from, each with typically 16 000 vectors. The typical error in each velocity component is about $7.4 \cos \phi_c \, \mathrm{m\,s^{-1}}$ in zonal velocity u, where ϕ_c is the planetocentric latitude, and about $7.4 \, \mathrm{m\,s^{-1}}$ in meridional velocity v. Dataset G14s is available for download from ORA-Data[44].

We also considered a third dataset S06[26], but this was not eventually used. Its correlation box is $3^\circ \times 3^\circ$ so its true resolution is relatively low. It contains many large gaps as wind vectors with meridional displacement greater than four pixels are filtered out, which excludes many large vortices including most of the Great Red Spot. Finally, the time separation between images is one rotation period (about $10 \, \mathrm{h}$) rather than an hour, which we found previously[27] to be too long to obtain good CIV matches.

Structure functions. For this calculation we used dataset G14s only. The structure function calculation cannot use our global mosaics as these combine velocities measured at different times, and hence there would be systematic errors associated with the evolution of the flow between images (up to one rotation period, around $10 \, \mathrm{h}$). Furthermore, there are systematic errors introduced in the mosaicing process by stitching together velocity fields valid at different times, particularly in the overlap regions. Therefore we did not compute structure functions from the G14g or C11 datasets. Structure functions calculated from dataset G14s use pairs of vectors from within the same image pair only, as these vectors are strictly valid at the same time and hence systematic errors associated with the evolution of the flow between images are avoided.

Structure functions were calculated following a method developed for Earth[20]. First we subtracted the time-zonal mean zonal $\langle u \rangle$ and meridional $\langle v \rangle$ velocities from each velocity vector, using this mean over the entire dataset in latitude bands of 0.5° (Supplementary Fig. 5). The time-zonal mean is the appropriate mean to subtract as the flow is assumed to be statistically steady, and the system is symmetrical about the planet's rotation axis. From the list of velocity vectors for a single image pair we selected a velocity vector and measured the great circle distance r to each of the other vectors in that image, along with the forward and back bearings[45]. For two velocity vectors $\mathbf{u}_1 = (u_1, v_1)$ at $\mathbf{x}_1 = (x_1, y_1)$ and $\mathbf{u}_2 = (u_2, v_2)$ at $\mathbf{x}_2 = (x_2, y_2)$, the longitudinal and transverse velocity differences are then

$$\delta u_L = (\mathbf{u}_2 - \mathbf{u}_1) \cdot \hat{\mathbf{n}} \qquad \delta u_T = (\mathbf{u}_2 - \mathbf{u}_1) \cdot \hat{\mathbf{t}} \tag{1}$$

where $\hat{\mathbf{n}} = \mathbf{r}/|\mathbf{r}|$ from $\mathbf{x}_1$ to $\mathbf{x}_2$, $\mathbf{r} = \mathbf{x}_2 - \mathbf{x}_1$. $\hat{\mathbf{n}}$ points along the forward bearing at each end (note that on the sphere $\hat{\mathbf{n}}$ will be different at the two ends). $\hat{\mathbf{t}} = \hat{\mathbf{n}} \times \hat{\mathbf{z}}$ in the northern hemisphere and $\hat{\mathbf{t}} = \hat{\mathbf{z}} \times \hat{\mathbf{n}}$ in the southern hemisphere both point perpendicular to $\mathbf{r}$, with $\hat{\mathbf{z}}$ the unit vector pointing away from the centre of the planet. Where $\mathbf{r}$ crossed the equator, its midpoint determined which $\hat{\mathbf{t}}$ to use.

δu_L and δu_T were calculated for every vector pair in every image, 9.1×10^9 vector pairs in total (Supplementary Fig. 6). We then split the data into bins of width $600 \, \mathrm{km}$ in r, chosen as a round number close to the typical separation between adjacent velocity vectors — about 0.5° or $610 \, \mathrm{km}$ along a great circle of radius a. Smaller bins produced aliasing between adjacent bins, particularly at low r, and larger bins began to smooth out detail in the structure function

Author post-print. Manuscript accepted for publication in *Nature Physics*.

at small r. Within each bin the mean δu_L^2, δu_T^2, δu_L^3, and $\delta u_L \delta u_T^2$ gave the 2nd and 3rd order structure functions. Averages were over all vector directions (we show structure functions for the East-West and North-South directions separately as Supplementary Fig. 7).

The best fits to the third order structure functions were found using a linear least squares fit. Confidence intervals in the fitting parameters and the structure functions were estimated using bootstrapping. The structure function was calculated using a combination of the vector pairs in each bin sampled randomly, with replacement, repeated 10 000 times to calculate 2.5–97.5% confidence intervals. The measured confidence intervals are around 4% (Fig. 2), but uncertainty due to the assumption of homogeneous isotropic turbulence in the fitting functions are likely to be significantly larger.

The results are presented on the sphere for better comparison with the spectral fluxes, but the same calculations done on (1) an oblate spheroid ($R_e = 71\,492\,\mathrm{km}$, $R_p = 66\,854\,\mathrm{km}$[46]), (2) assuming a locally flat surface for each image pair, and (3) taking a direct line between the start and end points through the planet and assuming no vertical velocity, all gave similar results. An image width of 60° on the sphere doesn't depart much from a locally flat surface; the arc and chord lengths for $r < 30\,000\,\mathrm{km}$ differ by less than 1%.

Spectral fluxes — global. Our spectral fluxes on the full sphere were calculated using a well-established technique used for Earth[10,11], using the Spherepack 3.0 library[47] to compute the spectral transforms and operations. This was done for datasets G14g and C11.

The spectral fluxes use the rotational (i.e. non-divergent) part of the flow $\mathbf{v}$ from a Helmholtz decomposition. This is the component $\mathbf{v} = \hat{\mathbf{z}} \cdot (\nabla \times \boldsymbol{\Psi})$ of the horizontal velocity field $\mathbf{u} = \mathbf{v} + \mathbf{w}$, for which $\nabla \cdot \mathbf{v} = 0$, where $\boldsymbol{\Psi}$ is the streamfunction. Similarly, the divergent (irrotational) component is $\mathbf{w} = \nabla\phi$, for which $\nabla \times \mathbf{w} = 0$, where ϕ is the velocity potential. At large scales 1-10% of the kinetic energy is in the divergent component in both datasets. At small scales, about 30–40% of the energy in C11 is in the divergent part, and 50–60% for G14g.

$\mathbf{v}$ was calculated first by performing a vector spherical harmonic analysis (Spherepack `vhaec`) on the full horizontal velocity field $\mathbf{u}$ to obtain the vorticity- and divergence-free velocity spectral coefficients $b_{m,n} = br_{m,n} + i\, bi_{m,n}$ and $c_{m,n} = cr_{m,n} + i\, ci_{m,n}$ respectively, where m and n are the zonal and total wavenumbers. Retaining the vorticity terms only the spectrum of the vorticity field[48] is $\omega_{m,n} = c_{m,n}\sqrt{n(n+1)}/a$. Similarly, the spectrum of the divergence field is $\delta_{m,n} = -b_{m,n}\sqrt{n(n+1)/a}$. The 1D kinetic energy spectrum is[10]

$$E_n = \sum_{m=-n}^{n} \frac{a^2}{4n(n+1)} \left[\omega_{m,n}\omega^*_{m,n} + \delta_{m,n}\delta^*_{m,n} \right] \tag{2}$$

where $*$ denotes the complex conjugate, which may be partitioned into rotational and divergent parts. Transforming $\omega_{m,n}$ back to real space (`ivrtec`) gives $\mathbf{v}$. The enstrophy transfer function (net enstrophy transfer from other wavenumbers into wavenumber n) is[11]

$$J_n = -\frac{1}{4} \sum_{m=-n}^{n} \left[\omega^*_{m,n} \left\{ \mathbf{v} \cdot \nabla\omega \right\}_{m,n} + \omega_{m,n} \left\{ \mathbf{v} \cdot \nabla\omega \right\}^*_{m,n} \right] \tag{3}$$

where ∇ is the horizontal gradient operator. Using a basic vector identity and $\nabla \cdot \mathbf{v} = 0$ we get $\mathbf{v} \cdot \nabla\omega = \nabla \cdot (\omega\mathbf{v})$. We multiplied $\mathbf{v}$ through by the vorticity field, computed its vector spherical harmonic analysis, and then calculated the spectrum of $\nabla \cdot (\omega\mathbf{v})$ by multiplying the divergent part of the $\omega\mathbf{v}$ spectrum by $-\sqrt{n(n+1)}/a$, from which we obtained J_n. The energy transfer function is then

$$I_n = \frac{a^2}{n(n+1)} J_n \tag{4}$$

and the enstrophy and energy fluxes are

$$H_{n+1} = -\sum_{l=1}^{n} J_l \qquad F_{n+1} = -\sum_{l=1}^{n} I_l \tag{5}$$

Author post-print. Manuscript accepted for publication in *Nature Physics*.

respectively.

To preprocess the G14g dataset for this calculation, first we filled in missing data by substitution as done previously[27]. The G14g grid and the grid Spherepack requires are offset by half a grid spacing in latitude, so the flux calculation was done twice, once using the points on the northern edge of the grid box, and once using the points on the southern edge. The difference was minimal. An interpolation across the grid box was not done as this artificially damped out flow features at the smallest scales.

For the C11 dataset, first we filled in undefined latitudes with zeroes. Points within 1.5° of the equator were removed due to the data processing method in the original analysis[28], and velocities were linearly interpolated across the gap. The C11 velocity fields are on a 0.05° grid (the pixel size in the original CB2 images), which over-samples the true resolution of the velocity field by about a factor of 10, as the correlation box used in the C11 CIV procedure was 10 pixels or 0.5° wide[28]. Therefore we subsampled the C11 data onto a 0.5° grid, by selecting every 10th point in longitude, and linearly interpolating to the required latitudes. The smoothing problem for G14g was not important as the interpolation was between two points separated by 0.05° rather than 0.5°. This gave ten semi-independent realisations of the subsampled velocity field, each one offset in longitude, so the C11 dataset effectively had 30 global velocity fields.

The spectral flux was calculated for each day and realisation separately, and then averaged at each wavenumber to find the mean flux and an estimate of the spread (shown in Supplementary Fig. 8).

Spectral fluxes — single images. Spectral fluxes from individual image pairs were estimated for dataset G14s using nonlinear triad interactions[29]. This provides an independent measurement of the spectral fluxes and allows us to estimate these fluxes without the systematic errors introduced by combining velocity fields into a global mosaic.

This method assumes Cartesian geometry so first we projected the positions of all the velocity vectors in a single image pair onto a locally flat plane centred around the latitude $\overline{\phi}$ and longitude $\overline{\lambda}$ of the centre of the image: $(x_i, y_i) = a((\lambda_i - \overline{\lambda})\cos\phi_i, \phi_i - \overline{\phi})$. Then we found the largest square that fit within the velocity field without leaving any gaps at the corners. The velocity field was interpolated onto a $N \times N$ grid with spacing $\Delta x = 2\pi a\,(\Delta\lambda/360)$ bounded by this square, using a smooth quintic polynomial interpolation to preserve as much of the small-scale information as possible. As for the global case, we used a $\Delta\lambda = 0.5^\circ$ grid spacing, which gives $\Delta x = 610\,\mathrm{km}$ and typically $N \approx 100$.

We transformed the velocity components u_{n_x,n_y} and v_{n_x,n_y} $[n_x, n_y = 0, \ldots, N-1]$ in real space to Fourier space. The spectral coefficients of the velocity components in terms of the 2D wavenumber $\mathbf{k} = (k_x, k_y)$ are

$$u_{n_x,n_y} = \sum_{k_y=0}^{N-1}\sum_{k_x=0}^{N-1} \tilde{u}_{k_x,k_y} \exp\left[i\frac{2\pi}{N}\Big(k_x n_x + k_y n_y\Big)\right] \tag{6}$$

and similarly for v_{n_x,n_y}, from which it follows[36] that the 2D spectral coefficients of vorticity, the rotational part of kinetic energy, and enstrophy[29] are

$$\tilde{\omega}_{k_x,k_y} = ik_x\tilde{v}_{k_x,k_y} - ik_y\tilde{u}_{k_x,k_y} \qquad \tilde{E}_{k_x,k_y} = \frac{\tilde{\omega}_{k_x,k_y}\tilde{\omega}^*_{k_x,k_y}}{2k^2} \qquad \tilde{\zeta}_{k_x,k_y} = \frac{\tilde{\omega}_{k_x,k_y}\tilde{\omega}^*_{k_x,k_y}}{2} \tag{7}$$

where $k = \sqrt{k_x^2 + k_y^2}$ is the 1D wavenumber, $k = 1$ corresponding to wavelength $N\Delta x$. To obtain the 1D energy spectrum at wavenumber k we then summed over all 2D energy coefficients $\tilde{E}_{k_x,k_y}$ where $k - \frac{1}{2} < \sqrt{k_x^2 + k_y^2} \le k + \frac{1}{2}$.

The spectral fluxes were calculated[29] from the 2D vorticity spectrum $\tilde{\omega}_{k_x,k_y}$, which is related to $\tilde{\Psi}_{k_x,k_y}$, the 2D stream function spectrum, by $\tilde{\omega}_{k_x,k_y} = -k^2\tilde{\Psi}_{k_x,k_y}$. In terms of the streamfunction the energy and enstrophy transfer functions between Fourier modes $\mathbf{k}$, $\mathbf{p} = (p_x, p_y)$, and $\mathbf{q} = (q_x, q_y)$, are[29]

$$T_{\mathbf{kpq}} = \mathcal{R}(-b_{\mathbf{kpq}}\tilde{\Psi}_{\mathbf{k}}\tilde{\Psi}_{\mathbf{p}}\tilde{\Psi}_{\mathbf{q}}) \qquad S_{\mathbf{kpq}} = k^2 T_{\mathbf{kpq}} \tag{8}$$

where $b_{\mathbf{kpq}}$ is an interaction coefficient. Writing this in terms of vorticity and expanding $b_{\mathbf{kpq}}$ we can write the transfer function as

$$T_{\mathbf{kpq}} = \frac{1}{2k^2}\left(\frac{1}{p^2} - \frac{1}{q^2}\right)(p_x q_y - q_x p_y)\,\delta(\mathbf{k} + \mathbf{p} + \mathbf{q})\,\tilde{\omega}_{\mathbf{k}}\,\tilde{\omega}_{\mathbf{p}}\,\tilde{\omega}_{\mathbf{q}} \tag{9}$$

Author post-print. Manuscript accepted for publication in *Nature Physics*.

where $p^2 = \mathbf{p}\cdot\mathbf{p}$ and $q^2 = \mathbf{q}\cdot\mathbf{q}$, and the δ-function reflects the fact that only triad interactions satisfying $\mathbf{k}+\mathbf{p}+\mathbf{q} = 0$ contribute to the transfer function. Note that only one $\mathbf{q}$ exists for each $[\mathbf{k}, \mathbf{p}]$ pair, which reduces the transfer function to $T_{\mathbf{kp}}$. We then obtain an energy transfer function T_{kp} in terms of the 1D wavenumbers k and p by summing over all triads satisfying $k - \frac{1}{2} < \sqrt{k_x^2 + k_y^2} \leq k + \frac{1}{2}$ and $p - \frac{1}{2} < \sqrt{p_x^2 + p_y^2} \leq p + \frac{1}{2}$. The enstrophy transfer function is $S_{kp} = k^2 T_{kp}$.

At wavenumber k the transfer function T_{kp} is positive for wavenumbers p that are giving energy to wavenumber k, and negative for wavenumbers that are taking away from wavenumber k. The spectral flux through a wavenumber k is obtained by summing over the 2D transfer function:

$$\Pi_k^E = + \sum_{k'=1}^{k} \sum_{p=1}^{k_{\max}} T_{k'p} \tag{10}$$

and similarly for enstrophy Π_k^Z. To match the sign of this quantity to the equivalent quantity on the sphere (equation 5), we reverse the sign of the original definition[29]. Flux from low to high wavenumbers (downscale) is positive, and flux from high to low wavenumbers (upscale) is negative. Here $k_{\max} = \frac{N}{2} - 1$ (N even) is the maximum 1D wavenumber that can be used to calculate triad interactions. Above this wavenumber we don't have the whole of (k_x, k_y) space available for a given 1D wavenumber. Typically $< 1\%$ of the energy is omitted from the calculation for this reason.

The spectra, transfer functions, and spectral fluxes were calculated for each of the image pairs. One of the image pairs (n1355320923 / n1355324709) was excluded from the analysis as it contained large gaps due to the moon Io passing in front of the planet. The mean and spread of fluxes over the 70 velocity fields was calculated (for spread, see Supplementary Fig. 8). As each image was a slightly different size (and hence $k = 1$ corresponded to slightly different distances in each case) averaging over the image pairs was done as a function of wavelength $\lambda = N\Delta x/k$ and then converted to an equivalent global wavenumber $n = 2\pi a/\lambda$.

Decomposition of the spectral fluxes. The spectral transfers (and fluxes) were decomposed into eddy-eddy interactions, zonal-zonal interactions (identically zero), and eddy-zonal interactions.

$$I_{m,n}^{\mathrm{tot}} = I_{m,n}^{\mathrm{ee}} + I_{m,n}^{\mathrm{zz}} + I_{m,n}^{\mathrm{ze}} \tag{11}$$

The eddy-zonal interactions were further decomposed into an eddy-zonal conversion and a zonal-eddy conversion.

$$I_{m,n}^{\mathrm{tot}} = I_{m,n}^{\mathrm{ee}} + C_{m,n}^{\mathrm{ez}} + C_{m,n}^{\mathrm{ze}} \tag{12}$$

This is based on an analogous decomposition into stationary and transient components[49]. $I_{m,n}^{\mathrm{ee}}$ was found by using eddy velocities in equations 3 and 9. The eddy-zonal energy conversion $C_{m,n}^{\mathrm{ez}}$ was calculated using eddy velocities for the terms in $\{\cdots\}$ in equation 3, and zonal velocities for the terms outside the brackets. In equation 9 the k term used its zonal component and the p and q terms their eddy components.

Code availability. The structure function and spectral flux code is available on request from R.M.B.Y. The Correlation Imaging Velocimetry software UVMAT/CIV used to create datasets G14g and G14s is maintained by Laboratoire LEGI, Grenoble.

Data availability. Raw images[33] are available from the NASA Planetary Data System Planetary Atmospheres Node (http://pds-atmospheres.nmsu.edu/). Dataset G14s[44] can be obtained from the Oxford University Research Archive — Data (https://ora.ox.ac.uk/). All other data supporting the findings of this study are available from the authors upon reasonable request.

[1] Porco, C. C. *et al.* Cassini Imaging of Jupiter's Atmosphere, Satellites, and Rings. *Science* **299**, 1541–1547 (2003).

Author post-print. Manuscript accepted for publication in *Nature Physics*.

[2] Ingersoll, A. P. *et al. Dynamics of Jupiter's atmosphere*, In Bagenal, F., Dowling, T. E. & McKinnon, W. B. (eds.) *Jupiter: The Planet, Satellites and Magnetosphere*, chap. 6, 105–128 (Cambridge University Press, 2004).

[3] Vasavada, A. R. & Showman, A. P. Jovian atmospheric dynamics: an update after Galileo and Cassini. *Reports Prog. Phys.* **68**, 1935–1996 (2005).

[4] Kolmogorov, A. N. The Local Structure of Turbulence in Incompressible Viscous Fluid for Very Large Reynolds Numbers (English translation 1991). *Proc. R. Soc. A* **434**, 9–13 (1941).

[5] Fjørtoft, R. On the Changes in the Spectral Distribution of Kinetic Energy for Twodimensional, Nondivergent Flow. *Tellus* **5**, 225–230 (1953).

[6] Kraichnan, R. Inertial Ranges in Two-Dimensional Turbulence. *Phys. Fluids* **10**, 1417–1423 (1967).

[7] Charney, J. Geostrophic turbulence. *J. Atmos. Sci.* **28**, 1087–1095 (1971).

[8] Salmon, R. Baroclinic instability and geostrophic turbulence. *Geophys. Astrophys. Fluid Dyn.* **15**, 167–211 (1980).

[9] Nastrom, G. D., Gage, K. S. & Jasperson, W. H. Kinetic energy spectrum of large- and mesoscale atmospheric processes. *Nature* **310**, 36–38 (1984).

[10] Boer, G. J. & Shepherd, T. G. Large-Scale Two-Dimensional Turbulence in the Atmosphere. *J. Atmos. Sci.* **40**, 164–184 (1983).

[11] Burgess, B. H., Erler, A. R. & Shepherd, T. G. The Troposphere-to-Stratosphere Transition in Kinetic Energy Spectra and Nonlinear Spectral Fluxes as Seen in ECMWF Analyses. *J. Atmos. Sci.* **70**, 669–687 (2013).

[12] Augier, P. & Lindborg, E. A New Formulation of the Spectral Energy Budget of the Atmosphere, with Application to Two High-Resolution General Circulation Models. *J. Atmos. Sci.* **70**, 2293–2308 (2013).

[13] Dewan, E. M. Stratospheric Wave Spectra Resembling Turbulence. *Science* **204**, 832–835 (1979).

[14] Lilly, D. K. Stratified Turbulence and the Mesoscale Variability of the Atmosphere. *J. Atmos. Sci.* **40**, 749–761 (1983).

[15] Tung, K. K. & Orlando, W. W. The k^{-3} and $k^{-5/3}$ Energy Spectrum of Atmospheric Turbulence: Quasi-geostrophic Two-Level Model Simulation. *J. Atmos. Sci.* **60**, 824–835 (2003).

[16] Tulloch, R. & Smith, K. S. A theory for the atmospheric energy spectrum: Depth-limited temperature anomalies at the tropopause. *Proc. Natl. Acad. Sci. U. S. A.* **103**, 14690–14694 (2006).

[17] Lindborg, E. Horizontal Wavenumber Spectra of Vertical Vorticity and Horizontal Divergence in the Upper Troposphere and Lower Stratosphere. *J. Atmos. Sci.* **64**, 1017–1025 (2007).

[18] Vallgren, A., Deusebio, E. & Lindborg, E. Possible Explanation of the Atmospheric Kinetic and Potential Energy Spectra. *Phys. Rev. Lett.* **107**, 268501 (2011).

[19] Lindborg, E. Can the atmospheric kinetic energy spectrum be explained by two-dimensional turbulence? *J. Fluid Mech.* **388**, 259–288 (1999).

[20] Cho, J. Y. N. & Lindborg, E. Horizontal velocity structure functions in the upper troposphere and lower stratosphere: 1. Observations. *J. Geophys. Res.* **106**, 10223–10232 (2001).

[21] King, G. P., Vogelzang, J. & Stoffelen, A. Upscale and downscale energy transfer over the tropical Pacific revealed by scatterometer winds. *J. Geophys. Res. Ocean.* **120**, 346–361 (2015).

[22] King, G. P., Vogelzang, J. & Stoffelen, A. Second-order structure function analysis of scatterometer winds over the Tropical Pacific. *J. Geophys. Res. Ocean.* **120**, 362–383 (2015).

Author post-print. Manuscript accepted for publication in *Nature Physics*.

[23] Scott, R. B. & Wang, F. Direct Evidence of an Oceanic Inverse Kinetic Energy Cascade from Satellite Altimetry. *J. Phys. Oceanogr.* **35**, 1650–1666 (2005).

[24] Tulloch, R., Marshall, J., Hill, C. & Smith, K. S. Scales, Growth Rates, and Spectral Fluxes of Baroclinic Instability in the Ocean. *J. Phys. Oceanogr.* **41**, 1057–1076 (2011).

[25] Ingersoll, A. P. *et al.* Interaction of Eddies and Mean Zonal Flow on Jupiter as Inferred from Voyager 1 and 2 Images. *J. Geophys. Res.* **86**, 8733–8743 (1981).

[26] Salyk, C., Ingersoll, A. P., Lorre, J., Vasavada, A. & Del Genio, A. D. Interaction between eddies and mean flow in Jupiter's atmosphere: Analysis of Cassini imaging data. *Icarus* **185**, 430–442 (2006).

[27] Galperin, B. *et al.* Cassini observations reveal a regime of zonostrophic macroturbulence on Jupiter. *Icarus* **229**, 295–320 (2014).

[28] Choi, D. S. & Showman, A. P. Power spectral analysis of Jupiter's clouds and kinetic energy from Cassini. *Icarus* **216**, 597–609 (2011).

[29] Maltrud, M. E. & Vallis, G. K. Energy and enstrophy transfer in numerical simulations of two-dimensional turbulence. *Phys. Fluids A* **5**, 1760–1775 (1993).

[30] Huang, H.-P., Galperin, B. & Sukoriansky, S. Anisotropic spectra in two-dimensional turbulence on the surface of a rotating sphere. *Phys. Fluids* **13**, 225–240 (2001).

[31] Scott, R. K. & Polvani, L. M. Forced-Dissipative Shallow-Water Turbulence on the Sphere and the Atmospheric Circulation of the Giant Planets. *J. Atmos. Sci.* **64**, 3158–3176 (2007).

[32] Porco, C. C. *et al.* Cassini Imaging Science: Instrument characteristics and anticipated scientific investigations at Saturn. *Space Sci. Rev.* **115**, 363–497 (2004).

[33] Vasavada, A. R., Porco, C. C. & The Cassini Imaging Science Team. NASA Planetary Data System: Cassini Cylindrical-Projection Maps near Jupiter Closest Approach (2008). URL `http://pds-atmospheres.nmsu.edu/Jupiter/CassiniMaps.txt`.

[34] Kolmogorov, A. N. Dissipation of Energy in the Locally Isotropic Turbulence (English translation 1991). *Proc. R. Soc. A* **434**, 15–17 (1941).

[35] Davidson, P. A. *Turbulence: An Introduction for Scientists and Engineers* (Oxford University Press, 2015), 2nd edn.

[36] Blazica, V., Zagar, N., Strajnar, B. & Cedilnik, J. Rotational and divergent kinetic energy in the mesoscale model ALADIN. *Tellus A* **65**, 18918 (2013).

[37] Gierasch, P. J. *et al.* Observation of moist convection in Jupiter's atmosphere. *Nature* **403**, 628–630 (2000).

[38] Ingersoll, A. P., Gierasch, P. J., Banfield, D., Vasavada, A. R. & The Galileo Imaging Team. Moist convection as an energy source for the large-scale motions in Jupiter's atmosphere. *Nature* **403**, 630–632 (2000).

[39] Blumen, W. Uniform Potential Vorticity Flow: Part I. Theory of Wave Interactions and Two-Dimensional Turbulence. *J. Atmos. Sci.* **35**, 774–783 (1978).

[40] Held, I. M., Pierrehumbert, R. T., Garner, S. T. & Swanson, K. L. Surface quasi-geostrophic dynamics. *J. Fluid Mech.* **282**, 1–20 (1995).

[41] Tulloch, R. & Smith, K. S. Quasigeostrophic Turbulence with Explicit Surface Dynamics: Application to the Atmospheric Energy Spectrum. *J. Atmos. Sci.* **66**, 450–467 (2009).

[42] Fincham, A. M. & Spedding, G. R. Low cost, high resolution DPIV for measurement of turbulent fluid flow. *Exp. Fluids* **23**, 449–462 (1997).

Author post-print. Manuscript accepted for publication in *Nature Physics*.

[43] Fincham, A. & Delerce, G. Advanced optimization of correlation imaging velocimetry algorithms. *Exp. Fluids* **29**, S13–S22 (2000).

[44] Young, R. M. B., Read, P. L., Armstrong, D. & Lancaster, A. J. Jupiter horizontal wind velocities at cloud level from Cassini [data-set]. Oxford: Oxford University Research Archive [distributor] `http://dx.doi.org/10.5287/bodleian:D5oVPJVRv` (2017).

[45] Williams, E. Aviation Formulary v1.46 (2011). URL `http://williams.best.vwh.net/avform.htm`.

[46] Seidelmann, P. K. *et al.* Report of the IAU/IAG Working Group on cartographic coordinates and rotational elements: 2006. *Celest. Mech. Dyn. Astron.* **98**, 155–180 (2007).

[47] Adams, J. C. & Swarztrauber, P. N. SPHEREPACK 3.0: A Model Development Facility. *Mon. Weather Rev.* **127**, 1872–1878 (1999).

[48] Adams, J. C. & Swarztrauber, P. N. SPHEREPACK 2.0 : A Model Development Facility. Tech. Rep. NCAR/TN-436+STR, NCAR (1997).

[49] Shepherd, T. G. A spectral view of nonlinear fluxes and stationary-transient interaction in the atmosphere. *J. Atmos. Sci.* **44**, 1166–1178 (1987).

Acknowledgments

Support for R.M.B.Y. provided by UK STFC Grant ST/K00106X/1. This work was supported in part by the US National Science Foundation under Grant No. NSF PHY11-25915. We are grateful to the the Leverhulme Trust for their support of the International Network on Waves and Turbulence. Raw images were made available by the Cassini Imaging Science Team via the NASA PDS Atmospheres Node. Datasets C11 and S06 were kindly provided by D. Choi and C. Salyk. We wish to thank P. Davidson, B. Galperin, G. King, B. Marston, M. McIntyre, H. Scolan, F. Tabataba-Vakili, S. Thomson, and A. Valeanu for useful discussions.

Author contributions

R.M.B.Y. wrote the code to calculate the structure functions and spectral fluxes, and performed the calculations. R.M.B.Y. wrote the bulk of the paper with sections on background and interpretation written by P.L.R. Both authors designed the research, decided on the methods used, and discussed the results.

Additional information

Supplementary information is available in the online version of the paper. Reprints and permissions information is available online at www.nature.com/reprints. Correspondence and requests for materials should be addressed to R.M.B.Y.

Competing financial interests

The authors declare that they have no competing financial interests.

Author post-print. Manuscript accepted for publication in *Nature Physics*.

Figure 1: **Sample image of Jupiter's clouds with jet scale and deformation radius.** This is part of a global mosaic of NASA Cassini ISS narrow-angle camera images combining the CB2 ($750\,\mathrm{nm}$) and BL1 ($451\,\mathrm{nm}$) filters. It shows a $45\times30°$ region of Jupiter's clouds centred at $130\,°\mathrm{W}$, $25\,°\mathrm{N}$. The approximate jet scale L_{jet} (corresponding to global wavenumber $n = 25$) and the estimated deformation radius L_D at $25\,°\mathrm{N}$ are shown. The zonal mean zonal velocity profile from dataset G14s is shown on the left; error bars (standard error in the mean at each latitude) are thinner than the line. Image credits: NASA/JPL/Space Science Institute/PIA07782.

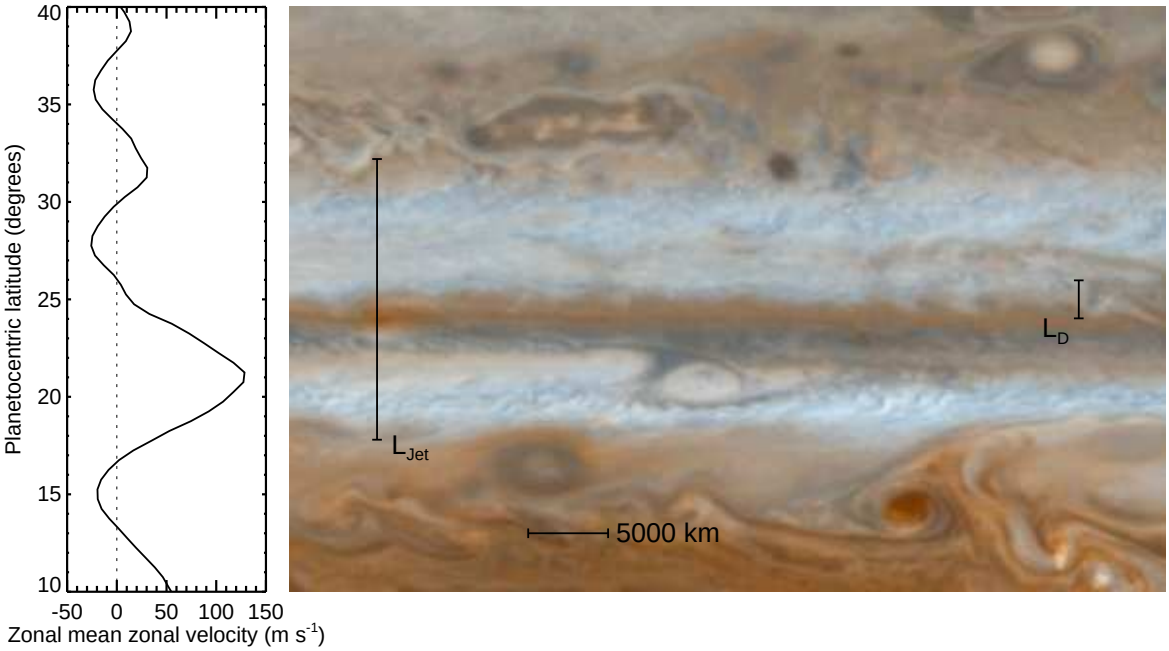

Author post-print. Manuscript accepted for publication in *Nature Physics*.

Figure 2: **Turbulent structure functions in Jupiter's weather layer.** **a**, 3rd order longitudinal (blue), transverse (red), and total (black) structure functions. Dashed grey lines are best linear fits to each, and dots are negative values. Thick lines show the mean for each function, and thin lines show the 95% confidence interval (whiskers for negative values) calculated using combinations of the vector pairs in each bin sampled randomly, with replacement, repeated $10\,000$ times. **b**, 2nd order longitudinal (blue), transverse (red), and total (black) structure functions. Confidence intervals are calculated in the same way as in **a**. The functions in both panels all use dataset G14s. Light grey shading shows the typical deformation radius L_D between latitudes 20-$40°$, and the jet scale. Above separation distance $r = 80\,000\,\mathrm{km}$ and below $r = 1500\,\mathrm{km}$ the separation vectors do not sample each possible direction (see Supplementary Fig. 6). The upper axes show the equivalent global wavenumber on the sphere $2\pi a/r$ for each separation distance, where $a = 69\,911\,\mathrm{km}$ is Jupiter's mean radius at $1\,\mathrm{bar}$.

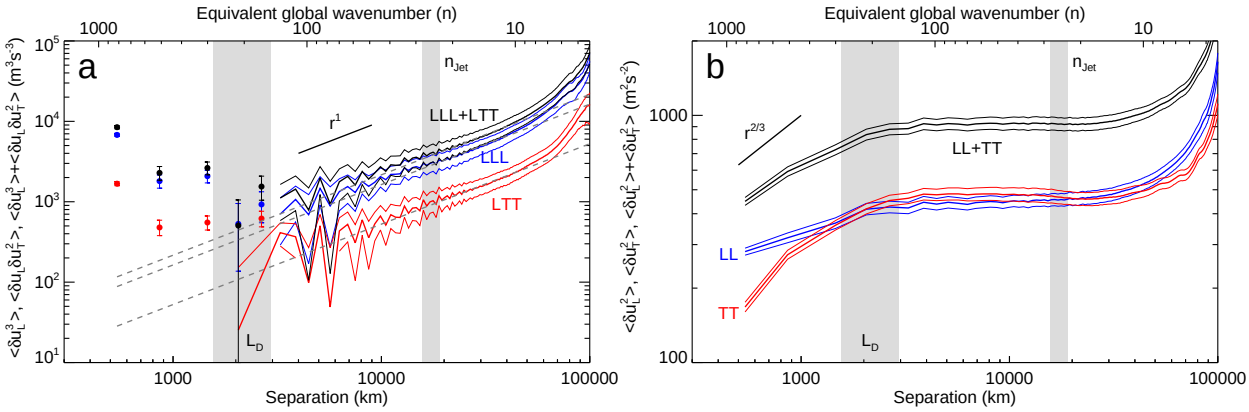

Author post-print. Manuscript accepted for publication in *Nature Physics*.

Figure 3: **Energy and enstrophy spectra and spectral fluxes in Jupiter's weather layer. a**, Eddy kinetic energy spectrum. **b**, Rotational (non-divergent) part of the eddy kinetic energy spectrum. **c**, Kinetic energy spectral flux computed from the non-divergent flow. **d**, As **c**, but for eddy-eddy interactions only. **e**, Eddy to zonal kinetic energy conversion. **f**, Enstrophy spectral flux. The three datasets are black (G14g), red (C11), and blue (G14s). Dataset G14s is scaled by various powers of 2π due to different definitions of the spectra and fluxes in different geometries. The lower axes show the approximately equivalent wavelength for each total wavenumber $\lambda = 2\pi a/n$. Light grey shading shows the jet scale and the typical deformation radius between latitudes 20-$40°$. See Supplementary Figs 8, 9, and 11 for error bars, Supplementary Fig. 12 for compensated eddy kinetic energy spectra, and Supplementary Fig. 13 for 2D kinetic energy and enstrophy spectra.

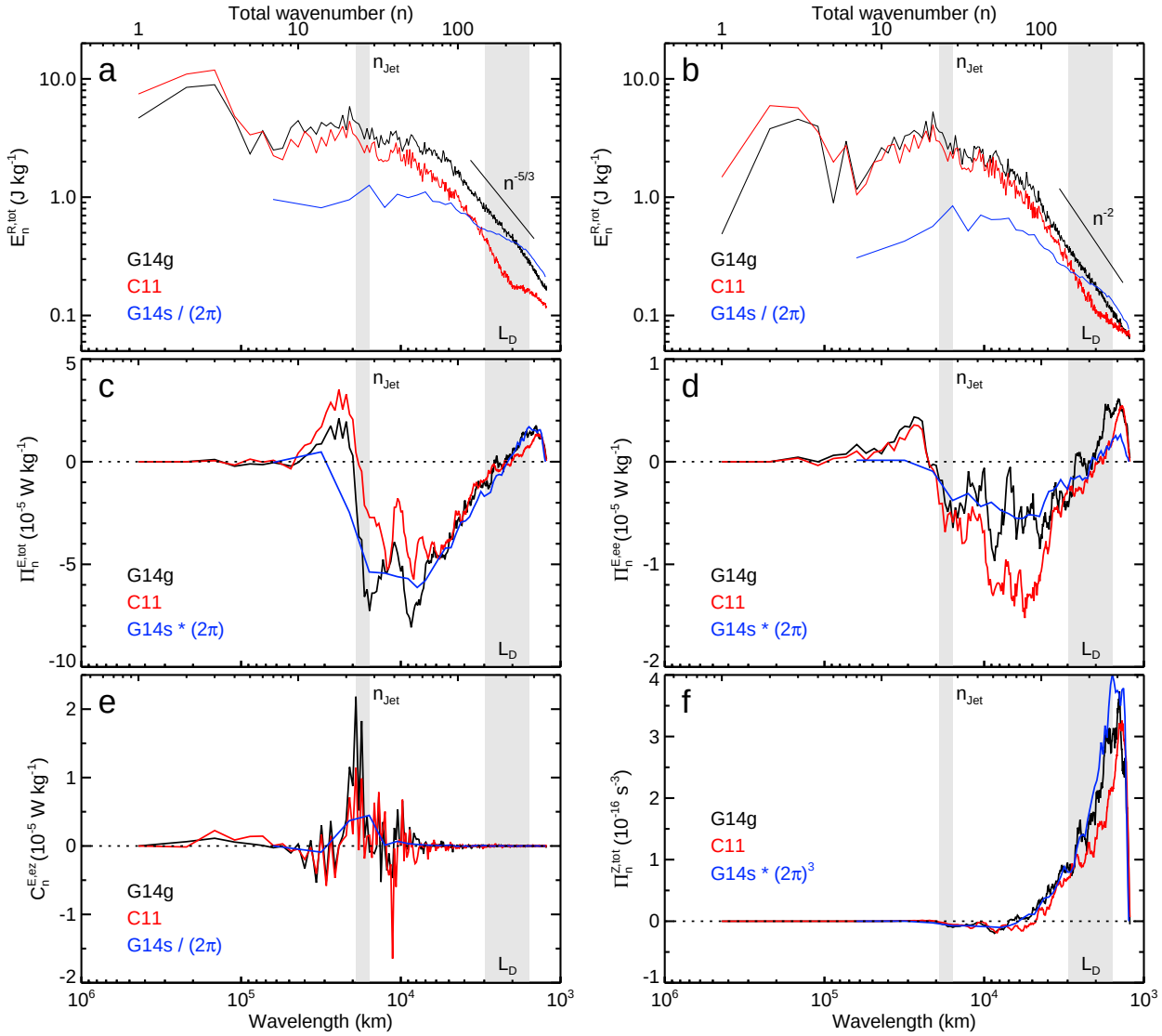

Author post-print. Manuscript accepted for publication in *Nature Physics*.